

Gaussian ray bundles for modeling high-frequency propagation loss under shallow-water conditions

Henry Weinberg

Naval Undersea Warfare Center Detachment, New London, Connecticut 06320-5594

Ruth Eta Keenan

Scientific Applications International Corp., Box 658, Mashpee, Massachusetts 02649

(Received 4 December 1995; accepted for publication 8 April 1996)

An acoustical propagation model was developed to analyze high-frequency propagation loss under shallow-water conditions. The model is based on Gaussian ray bundles which are similar in form but somewhat simpler than Gaussian beams. After describing the approach, propagation loss predictions are compared with those of various "standard models" at lower frequencies where the latter models are accurate and efficient. If Gaussian ray bundles compare well at the lower frequencies, they should perform well at the higher frequencies as ray approximations improve.

PACS numbers: 43.30.Cq [MBP]

INTRODUCTION

This paper introduces a range-dependent propagation loss model designed to support high-frequency simulations in shallow oceans. For simplicity, we confine our attention to a vertical (r, z) plane through the source and field points, and neglect out-of-plane scattering. The model uses Gaussian ray bundles of the form

$$\Psi = \frac{\beta_0 \Gamma^2}{\sqrt{2\pi\sigma p_r r}} \exp\{-0.5[(z - z_v)/\sigma]^2\}, \quad (1)$$

where β_0 depends only on the source, Γ includes losses due to volume attenuation and boundary reflections, z_v is the depth along a central ray, p_r is the horizontal slowness, and σ , an effective standard deviation or half-beamwidth, is given by

$$\sigma = \frac{1}{2} \max(\Delta z, 4\pi\lambda). \quad (2)$$

Here Δz is the change in ray depth at constant range due to a change in source angle $\Delta\theta_0$, and λ is the wavelength at the field point.

If $\Delta z > 4\pi\lambda$, σ confines most of the energy to the region between adjacent rays, while the $4\pi\lambda$ minimum aperture prevents the acoustic pressure from growing too large near caustics where

$$\lim_{\Delta\theta_0 \rightarrow 0} \frac{\Delta z}{\Delta\theta_0} = 0. \quad (3)$$

Equation (1) is based on conservation laws and appears to be consistent with Fresnel volume ray tracing.¹ Equation (2), on the other hand, was derived empirically during the development of a Gaussian beam model.² Gaussian ray bundles are somewhat easier to determine than Gaussian beams since σ is determined from adjacent rays at the field point, not by integrating differential equations. It is not known why the $4\pi\lambda$ in Eq. (2) performs as well as it does. Hence, the bundles should be used with caution until σ can be placed on a firmer foundation, or until another model can

be shown to provide a practical solution at the high frequencies of interest.

Several aspects of Gaussian ray bundles resemble the numerical integration of the one-way wide-angle Maslov–Chapman wavefield representation.³ For example, transforming the Helmholtz equation from depth dependence to vertical slowness leads to a modified eikonal equation. The solution, a Legendre transform from depth to vertical slowness, serves as an algorithm, Eq. (30), to extrapolate ray bundle travel time to a field point. An important difference is that our numerical integration of the pressure amplitude involves power (random phase) addition, not coherent transforms.

Hardy⁴ suggested that a Gaussian form involving an experimentally determined standard deviation could be used to treat caustics. Although critics argued that one would have to conduct a separate experiment for every case of interest, it now appears that the single expression, Eq. (2), is sufficient. This will be demonstrated by several heuristic arguments in Sec. I.

Sec. II contains two propagation loss test cases. The first compares results with those of the Navy standard PE v3.4 (Ref. 5) at 25 Hz and 10 kHz for a classic convergence zone. Then, the more academic model EFEPE⁶ is used to provide propagation loss at 1000 Hz for a shallow-water environment.

I. GAUSSIAN RAY BUNDLES

Our original intent was to evolve a ray-tracing program into a Gaussian beam model. Development by evolution often gives additional insight. In this instance, it led to Gaussian ray bundles. Since rigorous proofs are not currently available, the justification relies on heuristic arguments. We begin by using a brief discussion of classical ray theory as a vehicle to introduce the notation. Gaussian ray bundles are constructed from classical rays in a number of ways, four of which are described below. The basic technique applies to a benign environment in which there are sufficient classical

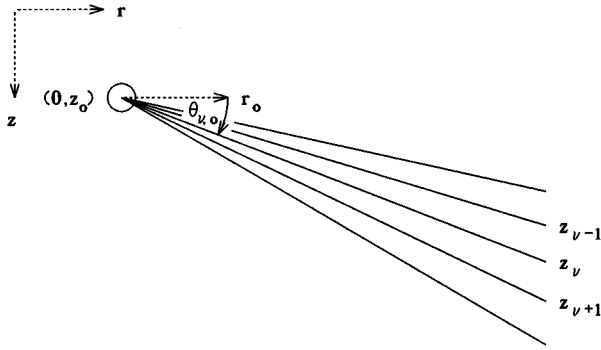


FIG. 1. Fan of acoustic rays launched from a point source.

rays of a desired ray type to form well-behaved differences. The second technique is a *fallback* procedure in case there is only one classical ray of a particular type in the region of interest. Virtual rays are defined by unfolding classical rays to model propagation in the vicinity of the ocean boundaries. The last technique modifies the basic formula to model propagation at short ranges.

First consider the fan of n rays in Fig. 1. Parameters that describe the ν th ray are subscripted by $(\cdot)_\nu$, while $(\cdot)_0$ refers to a point source with radian frequency ω at $(0, z_0)$. Accordingly, P_0 denotes the acoustic pressure at a reference distance r_0 from the source. The ν th ray is launched with source angle $\theta_{\nu,0}$ and crosses the field-point range r at depth z_ν and travel time T_ν . We define the horizontal and vertical slowness,

$$p_{r,\nu} = \cos \theta_\nu / c_\nu, \quad p_{z,\nu} = \sin \theta_\nu / c_\nu, \quad (4)$$

in terms of the horizontal inclination angle θ_ν and the sound speed c_ν . Losses due to volume attenuation and boundary reflections are simulated by the pressure ratio Γ_ν and phase shift Φ_ν . Recall that the vertex velocity $p_{r,\nu}^{-1}$ is a ray invariant in range-independent environments.

The numerical implementation of geometrical spreading will use finite differences to estimate Δz_ν , the increment in ray depth at constant range due to an increment in source angle $\Delta \theta_{\nu,0}$. For this discussion, it is sufficient to use the central differences

$$\Delta z_\nu = (z_{\nu+1} - z_{\nu-1})/2, \quad (5)$$

$$\Delta \theta_{\nu,0} = (\theta_{\nu+1,0} - \theta_{\nu-1,0})/2, \quad (6)$$

for $\nu = 2, 3, \dots, n-1$, and

$$\Delta z_1 = z_2 - z_1, \quad (7)$$

$$\Delta \theta_{1,0} = \theta_{2,0} - \theta_{1,0}, \quad (8)$$

$$\Delta z_n = z_n - z_{n-1}, \quad (9)$$

$$\Delta \theta_{n,0} = \theta_{n,0} - \theta_{n-1,0} \quad (10)$$

at the end points.

Later examples will demonstrate that the ocean boundaries will make the above definitions inappropriate for some

Δz_ν . In anticipation of these boundary-induced complications, we now introduce two depths, $z_\nu^{(1)}$ and $z_\nu^{(2)}$, that bound z_ν and set

$$\Delta z_\nu = z_\nu^{(2)} - z_\nu^{(1)}. \quad (11)$$

Equation (11) will be equivalent to Eqs. (5), (7), and (9) if the $z_\nu^{(1)}$ and $z_\nu^{(2)}$ are midpoints of the z_ν . That is

$$z_\nu^{(1)} = (z_{\nu-1} + z_\nu)/2, \quad (12)$$

for $\nu = 2, 3, \dots, n$, and

$$z_\nu^{(2)} = (z_\nu + z_{\nu+1})/2, \quad (13)$$

for $\nu = 1, 2, \dots, n-1$. The remaining depths,

$$z_1^{(1)} = (3z_1 - z_2)/2 \quad (14)$$

and

$$z_n^{(2)} = (3z_n - z_{n-1})/2, \quad (15)$$

are obtained by reflecting $z_1^{(2)}$ about z_1 and $z_n^{(1)}$ about z_n .

Under geometric-acoustic approximations, the contribution of the ν th ray to the total field can be estimated from

$$P_\nu = r_0 P_0 \Gamma_\nu \left| \frac{p_{r,\nu} r \Delta z_\nu}{p_{r,\nu,0} \Delta \theta_{\nu,0}} \right|^{-1/2} \exp(i\omega T_\nu + i\Phi_\nu) \quad (16)$$

if

$$z_\nu^{(1)} < z < z_\nu^{(2)}, \quad (17)$$

or if

$$z_\nu^{(2)} < z < z_\nu^{(1)} \quad (18)$$

and is zero otherwise. Each nontrivial P_ν corresponds to an eigenray, that is, a ray path that connects the source and field point. The underlying concept of classical ray theory is that the acoustic pressure P_c at any given field point is the coherent addition

$$P_c = \sum_\nu P_\nu \quad (19)$$

of eigenrays. The power addition (also known as random phase addition)

$$|P_r|^2 = \sum_\nu |P_\nu|^2 \quad (20)$$

is a smoother representation and better suited to many practical applications. Both summations include all nonzero values of P_ν .

We now define the amplitude of the ν th Gaussian ray bundle by

$$\Psi_\nu = \frac{\beta_{\nu,0} \Gamma_\nu^2}{\sqrt{2\pi} \sigma_\nu p_{r,\nu} r} \exp\{-0.5[(z - z_\nu)/\sigma_\nu]^2\}, \quad (21)$$

where

$$\beta_{\nu,0} = r_0^2 p_{r,\nu,0} \Delta \theta_{\nu,0} P_0^2 \quad (22)$$

depends only on the source,

$$\sigma_\nu = \frac{1}{2} \max(\Delta z_\nu, 4\pi\lambda) \quad (23)$$

is an effective standard deviation or half-beamwidth, and λ is the wavelength at the field point. The factor $\beta_{\nu,0}$ was chosen so that the energy within a geometric-acoustic ray tube equals the energy within a Gaussian ray bundle. Equation (23) was found empirically as will be described shortly.

If Eq. (16) is used, a classical eigenray is determined from a test ray that roughly falls within $\Delta z_\nu/2$ of the field-point depth at the field-point range. In contrast, ray bundles are global, affecting all depths to some degree. It is assumed that the Gaussian eigenray amplitude is formed by the power addition

$$\Psi_e = \sum_\nu \Psi_\nu \quad (24)$$

of bundles of the same type. The eigenray source angle $\theta_{e,0}$, horizontal slowness $p_{r,e}$, vertical slowness $p_{z,e}$, boundary phase shift Φ_e , and travel time T_e are obtained from the weighted averages:

$$\theta_{e,0} = \Psi_e^{-1} \sum_\nu \Psi_\nu \theta_{\nu,0}; \quad (25)$$

$$p_{r,e} = \Psi_e^{-1} \sum_\nu \Psi_\nu p_{r,\nu}; \quad (26)$$

$$p_{z,e} = \Psi_e^{-1} \sum_\nu \Psi_\nu p_{z,\nu}; \quad (27)$$

$$\Phi_e = \Psi_e^{-1} \sum_\nu \Psi_\nu \Phi_\nu; \quad (28)$$

$$T_e = \Psi_e^{-1} \sum_\nu \Psi_\nu T_{z,\nu}. \quad (29)$$

To obtain a more accurate expression for travel time, the ray bundle travel time T_ν is extrapolated to the field-point depth z by

$$T_{z,\nu} = T_\nu + p_{z,\nu}(z - z_\nu) \quad (30)$$

in Eq. (29) before the Gaussian weighting function is applied. The extrapolation in Eq. (30) is justified by the relationship

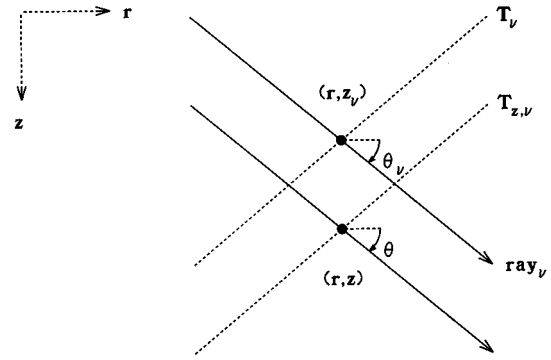


FIG. 2. CASS travel time extrapolation.

$$\frac{\Delta T_\nu}{\Delta z_\nu} \approx p_{z,\nu} \quad (31)$$

and Fig. 2. The Gaussian eigenray amplitude

$$A_e = \sqrt{\Psi_e} \quad (32)$$

and

$$\theta_e = \tan^{-1} \left(\frac{p_{z,e}}{p_{r,e}} \right) \quad (33)$$

yield the complex valued eigenray pressure

$$P_e = A_e \exp(i\omega T_e + i\Phi_e) \quad (34)$$

and field-point angle. An additional complication makes it necessary to compute two weighted averages for each ray type. The first is the contribution from ray bundles with $\Delta z_\nu > 0$, the second with $\Delta z_\nu \leq 0$. Ray bundles must be separated in order to simulate reversals in test ray depth versus source angle. These reversals are caustics that may be formed by the environment or by numerical approximations.

For simplicity, the current ray-tracing algorithm adds $-\pi/2$ to the phase Φ_ν at each upper and lower vertex. Asymptotic theory dictates that the eigenray phase shifts Φ_e corresponding to the $\Delta z_\nu > 0$ and $\Delta z_\nu \leq 0$ weighted averages

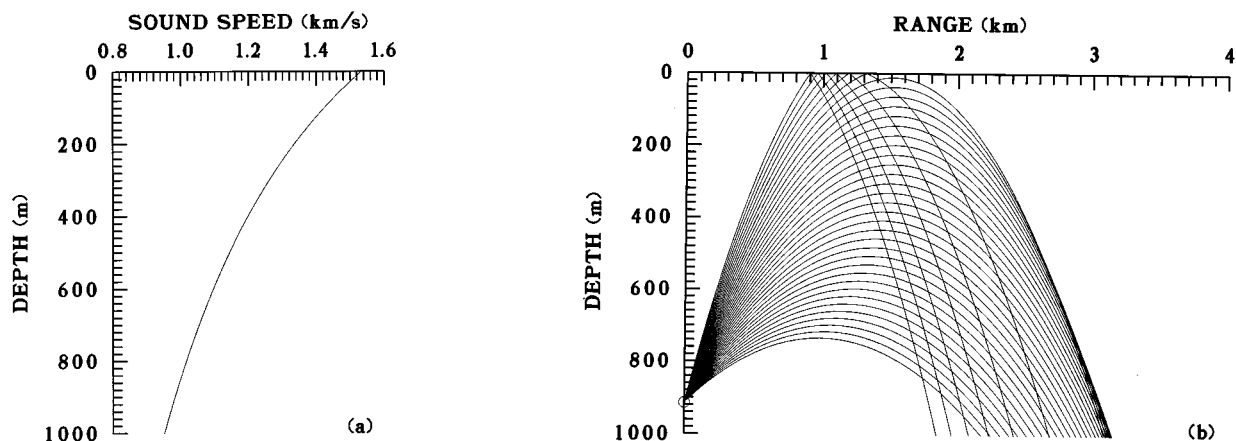


FIG. 3. Formation of a caustic under extreme downward refracting conditions: (a) Sound-speed profile, (b) Ray diagram for a 0.9144-km (1-kyd) source depth.

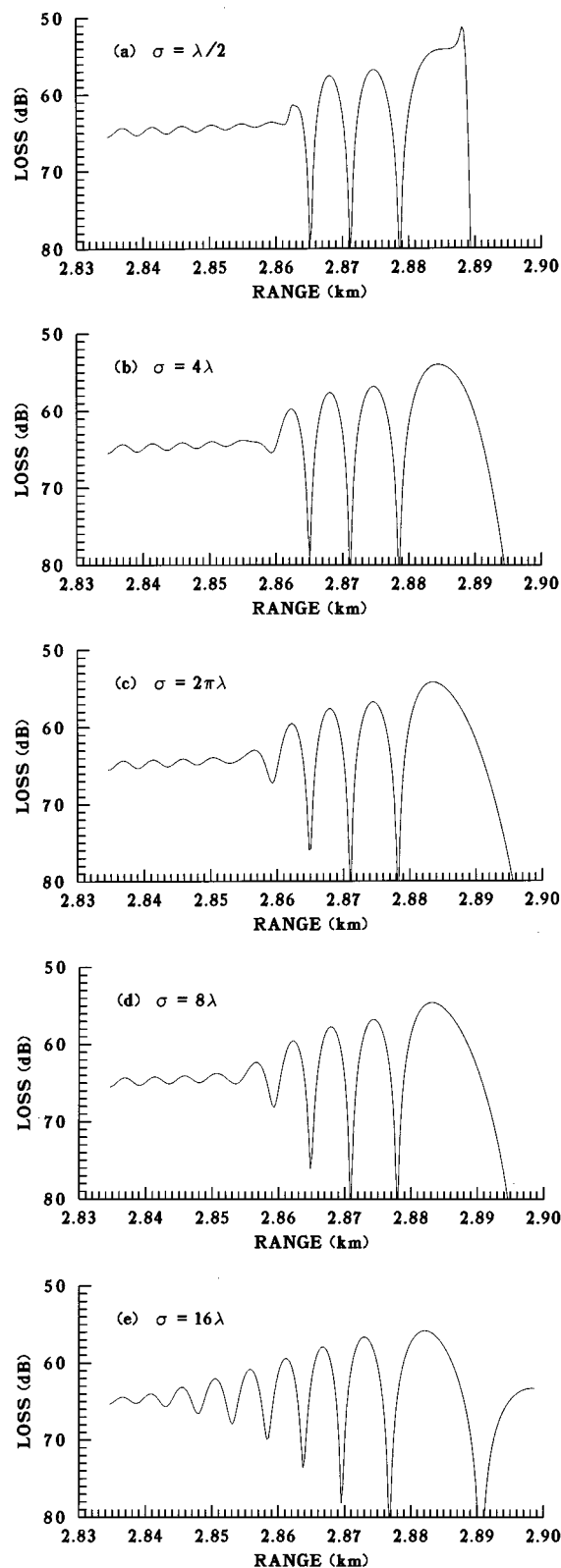


FIG. 4. Propagation loss versus range in the vicinity of a caustic for a 0.9144-km (1-kyd) source depth, 0.7315-km (0.8-kyd) field-point depth, and various lower bounds of σ_v : (a) $\lambda/2$, (b) 4λ , (c) $2\pi\lambda$, (d) 8λ , (e) 16λ .

be separated by an additional $\pi/2$. These assumptions are not valid in many environments, and the coherent predictions are subject to errors.

The standard deviations σ_v must be bounded from below in order to prevent the amplitudes Ψ_v from growing too large

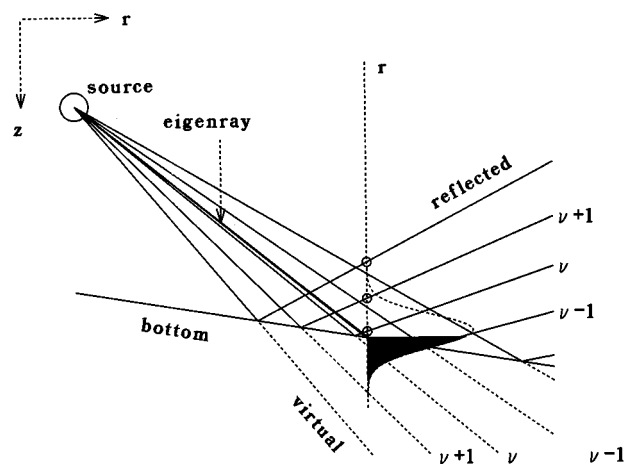


FIG. 5. Creation of virtual rays by unfolding classical rays at a boundary.

in the vicinity of caustics. This bound will now be estimated for a well-known test case developed by Pederson and Gordon⁷ to investigate extreme downward refraction. Figure 3 contains their sound-speed profile and ray diagram for a 0.9144-km (1-kyd) source depth. The inverse sound-speed squared is linear in depth, so one can express ray trajectories in closed form. However, the results below do not use this feature and may be contaminated to a small degree by numerical artifacts. It should also be noted that the example does not represent realistic ocean conditions in that the sound speed is too small throughout most of the water column.

Figure 4 illustrates the effect of changing the lower bound of σ on propagation loss for a 0.7315-km (0.8-kyd) field-point depth in the vicinity of the caustic at 2.89 km. Decibel levels were computed by coherent addition for various lower bounds of σ_v . In Fig. 4(a), σ_v is too small. Although bounded, the level is too high in the illuminated region to the left of the caustic and falls off too rapidly in the shadow zone to the right of the caustic. The opposite occurs in Fig. 4(e), where σ_v is too large; now the decibel level is too small at the caustic, and falls off too slowly in the shadow zone. Equation (23) is currently based on Fig. 4(c). Evidence to be provided later will indicate that this remarkably simple formula is far more general than one would expect.

As is customary in typical ray-tracing models, rays are attenuated at the ocean boundaries by appropriate reflection coefficients. The cumulative effect is contained in the pressure ratio Γ_v and phase shift Φ_v . Specific examples of reflection coefficients appear in later sections. The ocean boundaries impose additional requirements on the numerical computation of both classical and Gaussian eigenrays. Although the difficulties discussed below stem from tracing rays to a constant range, it is felt that the benefits of *stepping* in range overshadow any disadvantages.

First consider a constant sound speed environment. The range r and field point to source depth $z - z_0$ for the direct path are related by

$$z - z_0 = r \tan \theta_0. \quad (35)$$

Holding r constant, the differential

$$dz = r \sec^2 \theta_0 d\theta_0 \quad (36)$$

provides the lower bound

$$\Delta z_\nu \geq r \Delta \theta_{\nu,0} \quad (37)$$

for the change in ray depth with source angle. In other words, if the angular spacing between test rays is too large, there will be only one direct path at the range of interest. It will not be possible to compute the required increments Δz_ν and $\Delta \theta_{\nu,0}$. Realistic ocean conditions create additional complications.

If computer run time is not a concern, and the sound speed and bottom are well behaved, one can make $\Delta \theta_{\nu,0}$ sufficiently small so that several rays of the same type cross the range of interest. The practical approach taken here uses

$$z_\nu^{(1)} = z_\nu - \Delta z_\nu/2, \quad z_\nu^{(2)} = z_\nu + \Delta z_\nu/2, \quad (38)$$

instead of Eqs. (12), (13), (14), and (15) to set the bounding depths $z_\nu^{(1)}$ and $z_\nu^{(2)}$, where

$$\Delta z_\nu = z_b - z_s \quad (39)$$

is the difference between the bottom and surface depths at range r . Since adjacent rays of the same type are unavailable, the Gaussian bundle distributes its energy normally about the central ray with a standard deviation of half the water column.

It is often possible to create adjacent rays of a desired type by unfolding rays of an adjacent type. To demonstrate the importance of these virtual rays, consider an eigenray that is incident to a field point slightly above the ocean bottom as shown in Fig. 5. Circles along the vertical dashed line represent the depths at which a fan of reflected test rays cross the field point range r , with ray ν being the closest to the bottom. Besides denoting range, the horizontal axis also serves to illustrate the relative amplitude of a Gaussian ray bundle that is centered at z_ν and has a standard deviation of $\sigma = |\Delta z_\nu|/2$. The unshaded portion represents reflected energy that does not contribute to the incident eigenray. Unless unfolded, power due to the shaded portion will be lost to the bottom; the eigenray's amplitude will be too small. By projecting the bundle along incident rays, it becomes clear that the shaded portion corresponds to incident energy.

Except in the simplest cases, it is not clear how the virtual ray parameters $\theta'_{\nu,0}$, $p'_{r,\nu}$, $p'_{z,\nu}$, Φ'_ν , T'_ν , and Ψ'_ν

should be unfolded from their real counterparts. In order to avoid the cumbersome task of adding or removing the effects of boundary reflection coefficients during the unfolding process, the current procedure sets

$$\begin{aligned} \theta'_{\nu,0} &= \theta_{\nu,0}, & p'_{r,\nu} &= p_{r,\nu}^*, \\ p'_{z,\nu} &= p_{z,\nu}^*, & \Psi'_\nu &= \Psi_\mu, \\ T'_\nu &= T_\nu, & \Phi'_\nu &= \Phi_\mu, \end{aligned} \quad (40)$$

where the asterisk (*) indicates a reflection about the appropriate boundary and μ is the ray index nearest to ν such that ray μ and the eigenray are of the same type. Errors in virtual ray parameters increase with distance to the boundary. However, the distance from the virtual ray to the field point also increases, so that the effect on the eigenray decreases.

For example, referring once again to Fig. 5, we see that $(p'_{r,\nu}, p'_{z,\nu})$ are the direction numbers of the dashed line for ray ν . The virtual ray amplitude and phase are obtained from ray $\mu = \nu - 1$, the direct path ray nearest to ray ν .

A few other special cases require special attention. For brevity, we limit the discussion to one, near-field propagation. For the amplitude of the Gaussian ray bundle Ψ_ν to approach spherical spreading as the field point $(r, z) \rightarrow (0, z_0)$, it is necessary that the standard deviation

$$\sigma_\nu \propto \Delta z_\nu \quad (41)$$

in the vicinity of the source. Unless Eq. (23) is adjusted, Eq. (37) indicates that the $2\pi\lambda$ lower bound of σ_ν will be invoked for short ranges such that

$$r \leq \frac{\Delta z_\nu}{\Delta \theta_{\nu,0}} \leq \frac{4\pi\lambda}{\Delta \theta_{\nu,0}}. \quad (42)$$

The current adjustment replaces the $4\pi\lambda$ in Eq. (23) by

$$\min\left(\frac{\pi r}{180}, 4\pi\lambda\right). \quad (43)$$

One degree or $\pi/180$ rad was found to work better than $\Delta \theta_{\nu,0}$ in several test cases.

II. MODEL COMPARISONS

This section contains two sets of propagation loss test cases. For convenience, the Gaussian ray bundle computer

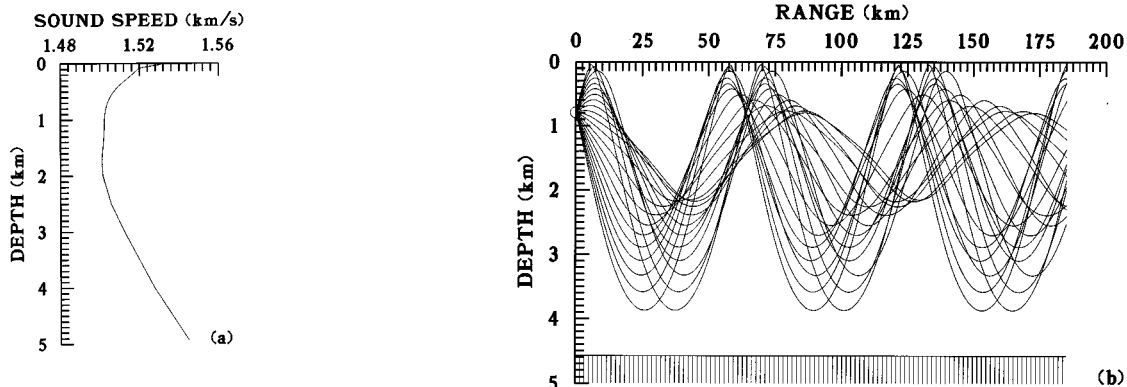


FIG. 6. Classic CZ environment: (a) sound-speed profile and (b) ray trace.

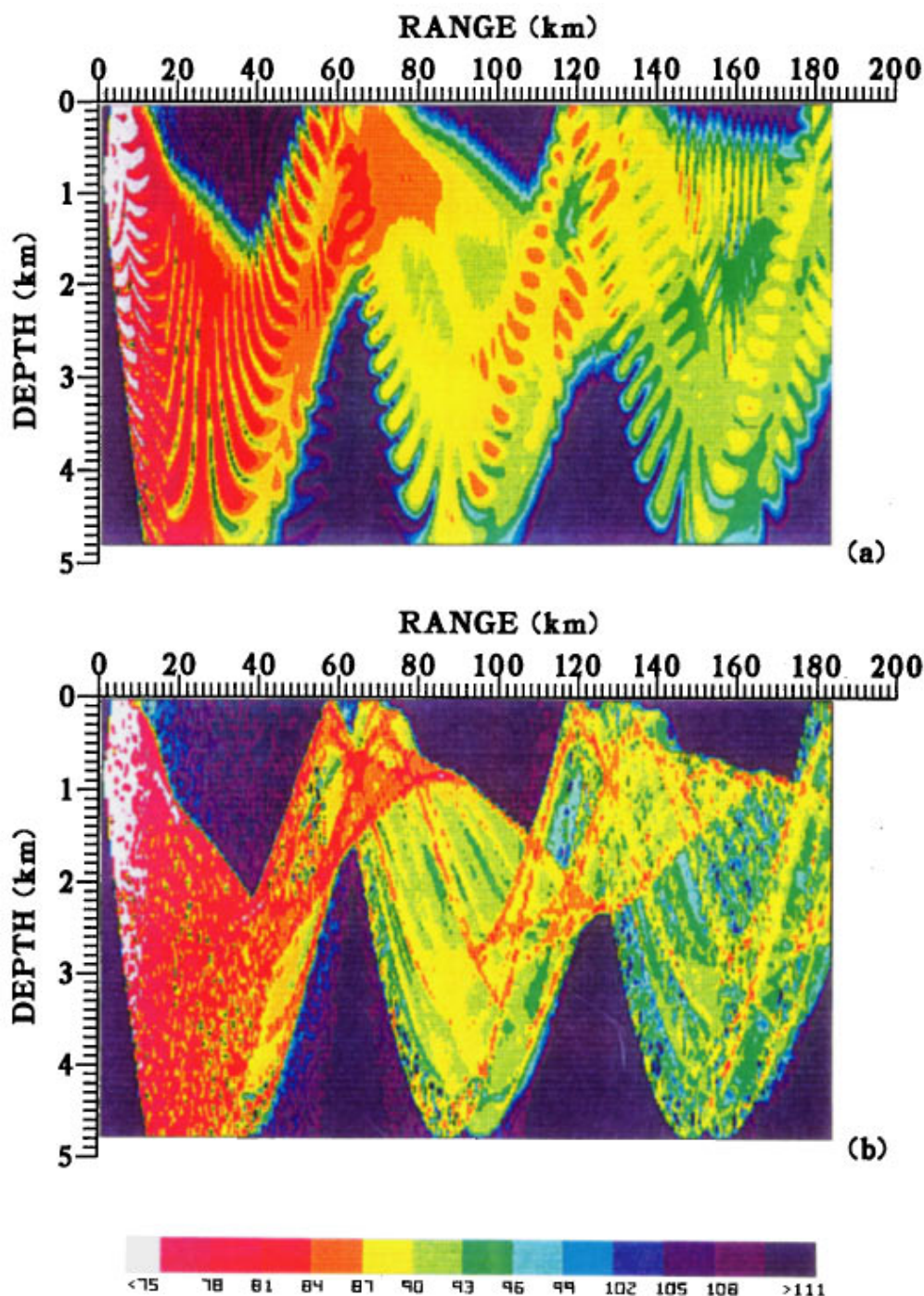


FIG. 7. GRAB propagation loss contours for classic CZ environment: (a) 25 Hz and (b) 10 kHz.

code has been given the acronym GRAB. The first test case compares GRAB results with those of the Navy standard PE v3.4 (Ref. 5) at 25 Hz and 10 kHz for a classic convergence zone. Then GRAB and the more academic model EFEPE (Ref. 6) are used to predict propagation loss at 1000 Hz for a shallow-water environment. If GRAB compares well at these lower frequencies, it should also perform well above 20 kHz, the high frequencies of interest.

To avoid model/model comparison complications, the same submodels (surface loss, bottom loss, etc.) were used whenever possible. Since the bottom descriptions required by GRAB and EFEPE are sufficiently different, it was nec-

essary to generate a plane-wave coefficient from bottom layers and implement these into a GRAB bottom loss table. Range-dependent sound speed is not resolved so easily.⁸ PE and EFEPE transition abruptly from one profile to another at user-provided ranges. Only GRAB models the sound speed continuously with range.

A. Classic convergence zone

We will now compare GRAB predictions for a classic convergence zone with those of the Navy standard model PE v3.4. The sound-speed profile and ray trace for a 792.48-m (2600-ft) source depth and 13 716-m (15 000-ft) water depth

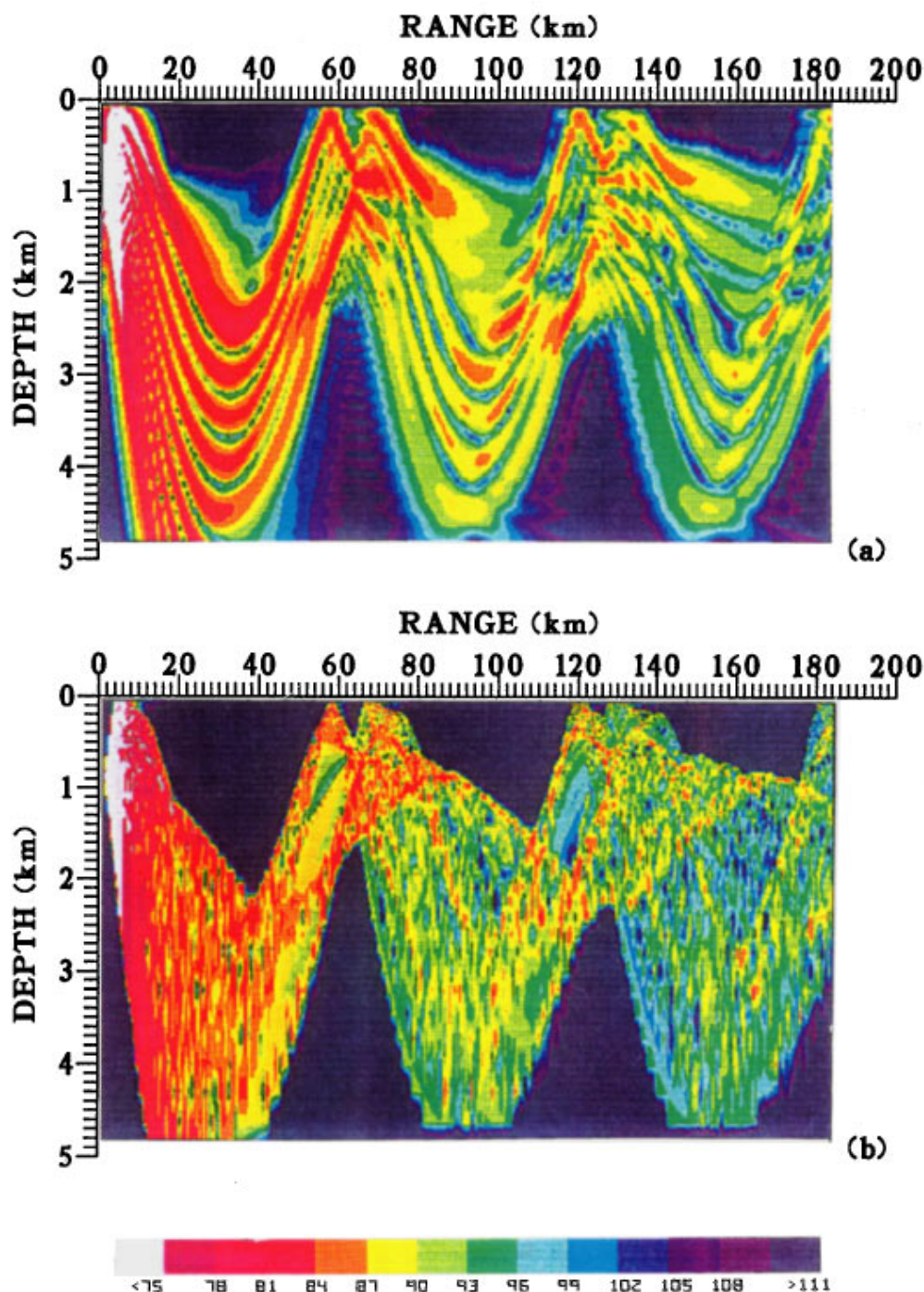


FIG. 8. PE propagation loss contours for classic CZ environment: (a) 25 Hz and (b) 10 kHz.

appear in Fig. 6. GRAB and PE 25-Hz and 10-kHz propagation losses are contoured in Figs. 7 and 8, respectively. To highlight the formation of shadow zones and caustics, GRAB and PE were run without volume attenuation or bottom interacting energy. GRAB used power addition, sampled range in 1.852-km (1-nmi) increments and employed a $\pm 20^\circ$ vertical aperture in 0.1° increments. The full-field PE model automatically selects sampling parameters to avoid aliasing.

Figure 9 displays GRAB and PE propagation loss versus range at a 792.48-m (2600-ft) receiver. Although GRAB was not designed for frequencies as low as 25 Hz, the model

tracks the general trend and maintains energy levels in the tails of the caustic. The GRAB computation time for each frequency was 4.5 min using a 50-MHz 386 IBM personal computer. PE required 6 s and 26 h for the 25-Hz and 10-kHz cases, respectively.

B. Shallow-water environment at 1000 Hz

The next set of cases compares GRAB and EFEPE for a shallow-water environment. Due to high-frequency computation requirements of EFEPE, it was convenient to make the

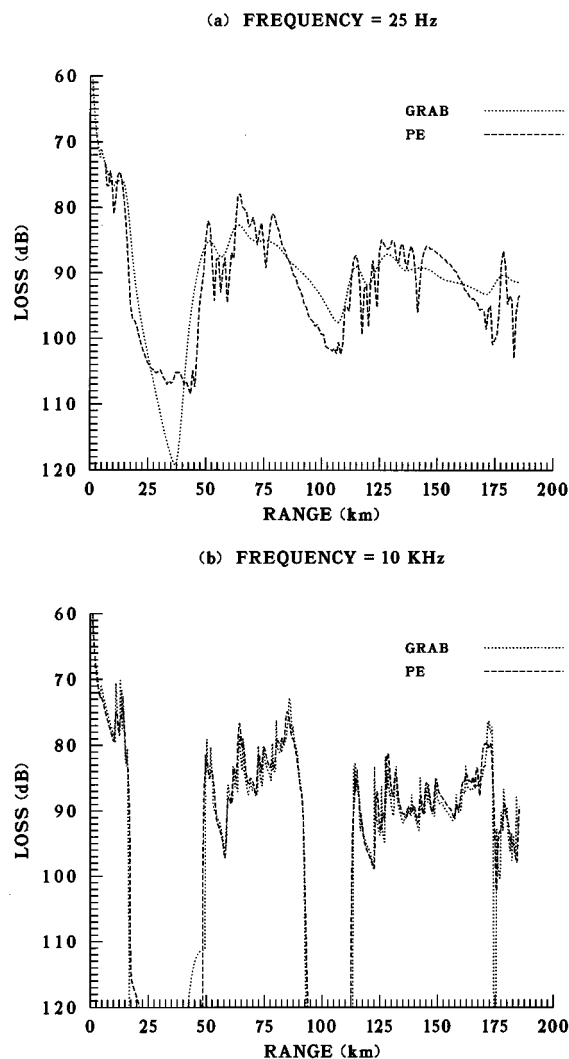


FIG. 9. GRAB and PE propagation loss predictions at a 792.48-m (2600-ft) receiver in a classic CZ environment: (a) 25 Hz and (b) 10 kHz.

comparison at 1000 Hz. Our assumption was that the essential physics at 1000 Hz is the same as at 20 kHz, and that differences can be attributed to volume and boundary losses whose accuracy is independent of the propagation model. For the model/model comparisons here, the environment consists of the sound-speed profile in Fig. 10, a perfectly

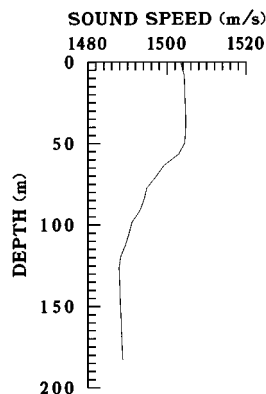


FIG. 10. Shallow-water environment sound-speed profile.

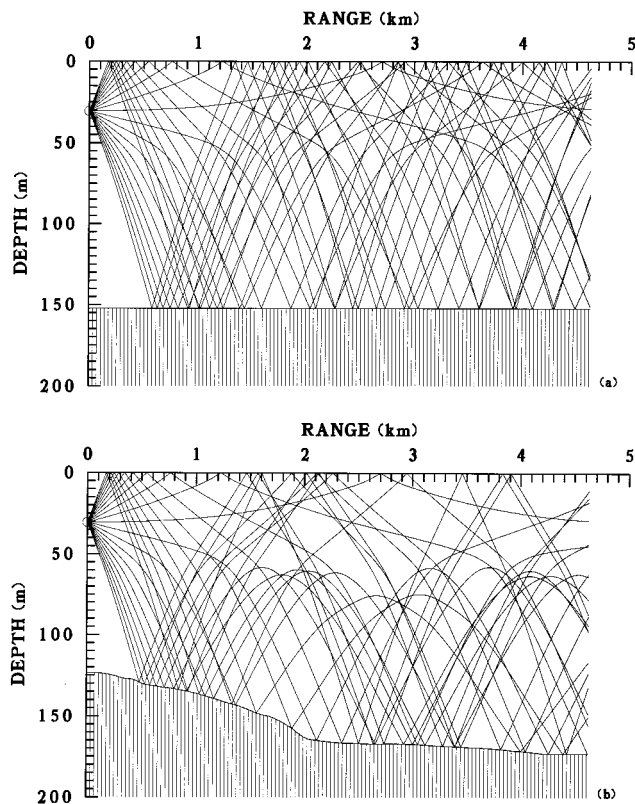


FIG. 11. Shallow-water environment ray trace: (a) flat 152.4-m (500-ft) and (b) downslope bathymetry.

reflecting sea surface, and zero volume attenuation. The source and receiver depths are 30.48 m (100 ft). Predictions were made for a flat bottom at 152.4 m (500 ft) of all sand or all rock, and for a downslope bathymetry. Ray diagrams for both bathymetries are traced in Fig. 11.

1. Sand bottom

The sand bottom parameters include a 1572-m/s sediment sound speed, a 1.268-g/cm³ density, and an attenuation

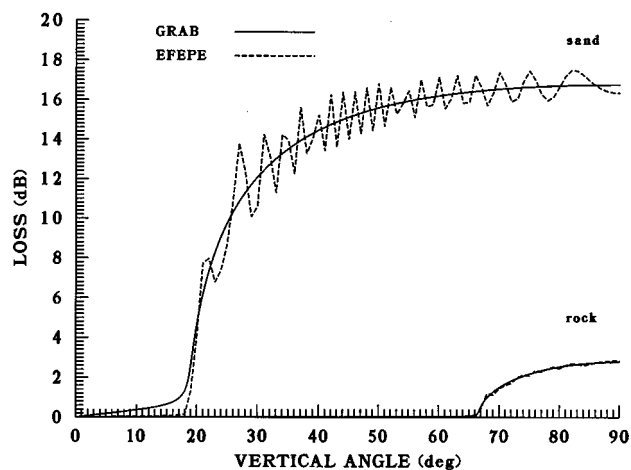


FIG. 12. Bottom forward reflection loss versus angle at 1 kHz for sand and rock.

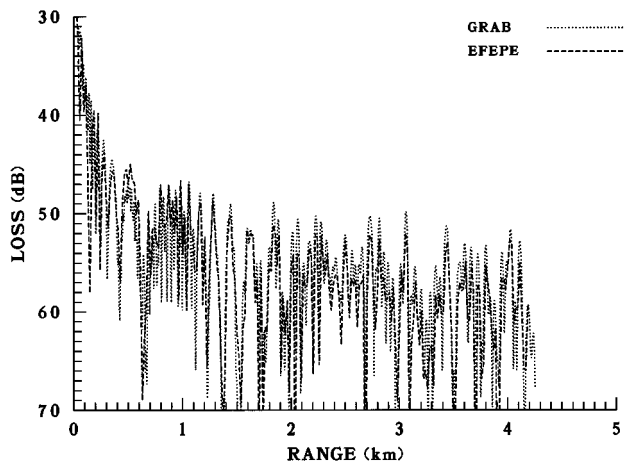


FIG. 13. Coherent GRAB and EFEPE propagation loss predictions at 1 kHz for a flat sandy bottom.

of 0.02 dB/ λ or 0.03 dB at 1000 Hz. These yield the bottom loss versus grazing angle curves in the upper portion of Fig. 12. GRAB exercised its Rayleigh reflection coefficient option, while EFEPE computed equivalent plane-wave reflection coefficients for a two-layered bottom.

Figure 13 compares the coherent GRAB prediction with those of EFEPE. The GRAB range step is 10 m and its aperture is $\pm 80^\circ$ with test rays every 0.1° . EFEPE used a 1.5-m range step and a 0.1-m depth mesh. The GRAB levels differ from the EFEPE levels by less than 1 dB at most ranges. Note the exceptional agreement between interference patterns.

2. Rock bottom

The rock bottom is described by a 3750-m/s sound speed, a 0.02-dB/ λ attenuation, and 2.5-g/cm³ sediment density. GRAB and EFEPE bottom forward reflection loss for a rock bottom are shown in the lower portion of Fig. 12. Although sand bottom losses for grazing angles beyond 20° are highly attenuated, propagation over rock is strong for grazing angles up to 67° . In this test case, an 80° source angle inter-

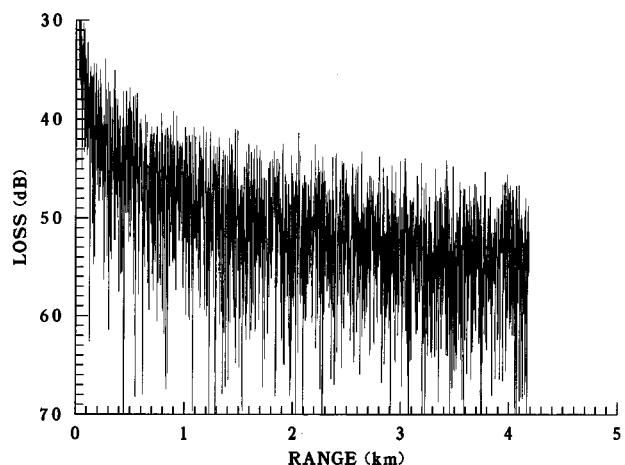


FIG. 14. GRAB coherent propagation loss predictions at 1 kHz for a flat rocky bottom.

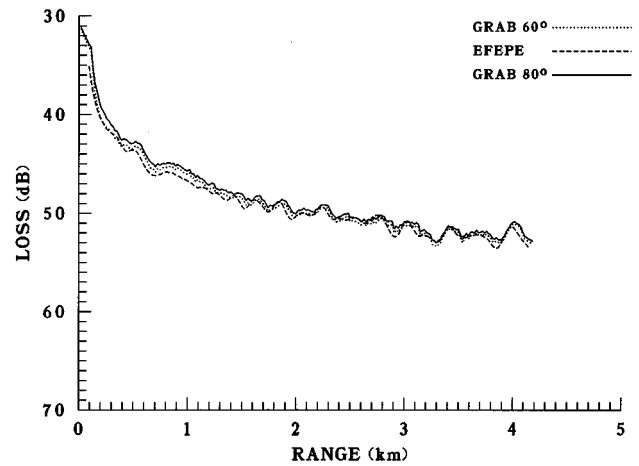


FIG. 15. GRAB and EFEPE range averaged propagation loss predictions at 1 kHz for a flat rocky bottom.

acted with the bottom 50 times in 2.6 km. Thus small differences in the bottom description become significant. Figure 14 illustrates GRAB coherent predictions with a 1-m range step and a $\pm 80^\circ$ aperture sampled every 0.1° . Because angles up to 80° are now important, the interference pattern is more complicated than it was for the sand bottom. To make meaningful comparisons, the intensity is averaged over a 0.1852-m (0.1-nmi) sliding range window. Figure 15 displays the results every 0.01852 m (0.01 nmi). As in the sand bottom case, EFEPE was run with a range step of 1.5 m and a depth mesh of 0.1 m. Even with its better phase modeling, EFEPE results have phase errors due to high propagation angles. Nevertheless, differences between the range-averaged GRAB and EFEPE predictions are small.

3. Rock to sand for variable bottom depth

The actual scenario that prompted this series of tests was a downslope run where the bottom properties changed from rock to sand. Figure 11 shows that the slope redirects energy away from the surface duct. First consider the effect of the slope with an all sand bottom. Figure 16 shows GRAB propagation loss contours for the flat 152.4 m and downslope bathymetries. As the ray trace Fig. 11 indicates, the overall levels at the 30.48-m receiver are lower when the bottom slopes downward.

Note that the coherent propagation losses at the 30.48-m receiver predicted by GRAB and EFEPE in Fig. 17 transition from rapid fluctuations over the rock bottom to slower fluctuations over sand. Little difference is seen in propagation loss levels over the rock (where the bottom is still relatively flat), but significant differences are seen between models over the sloping sand bottom at 2.315 km. Figure 18 compares 0.01852-m range-averaged GRAB and EFEPE predictions. Finally, Fig. 19 shows power-addition and range-averaged GRAB predictions at 21 kHz. The 1- and 21-kHz predictions are similar because the bottom loss is nearly the same for the two frequencies, and neither has surface or volume losses.

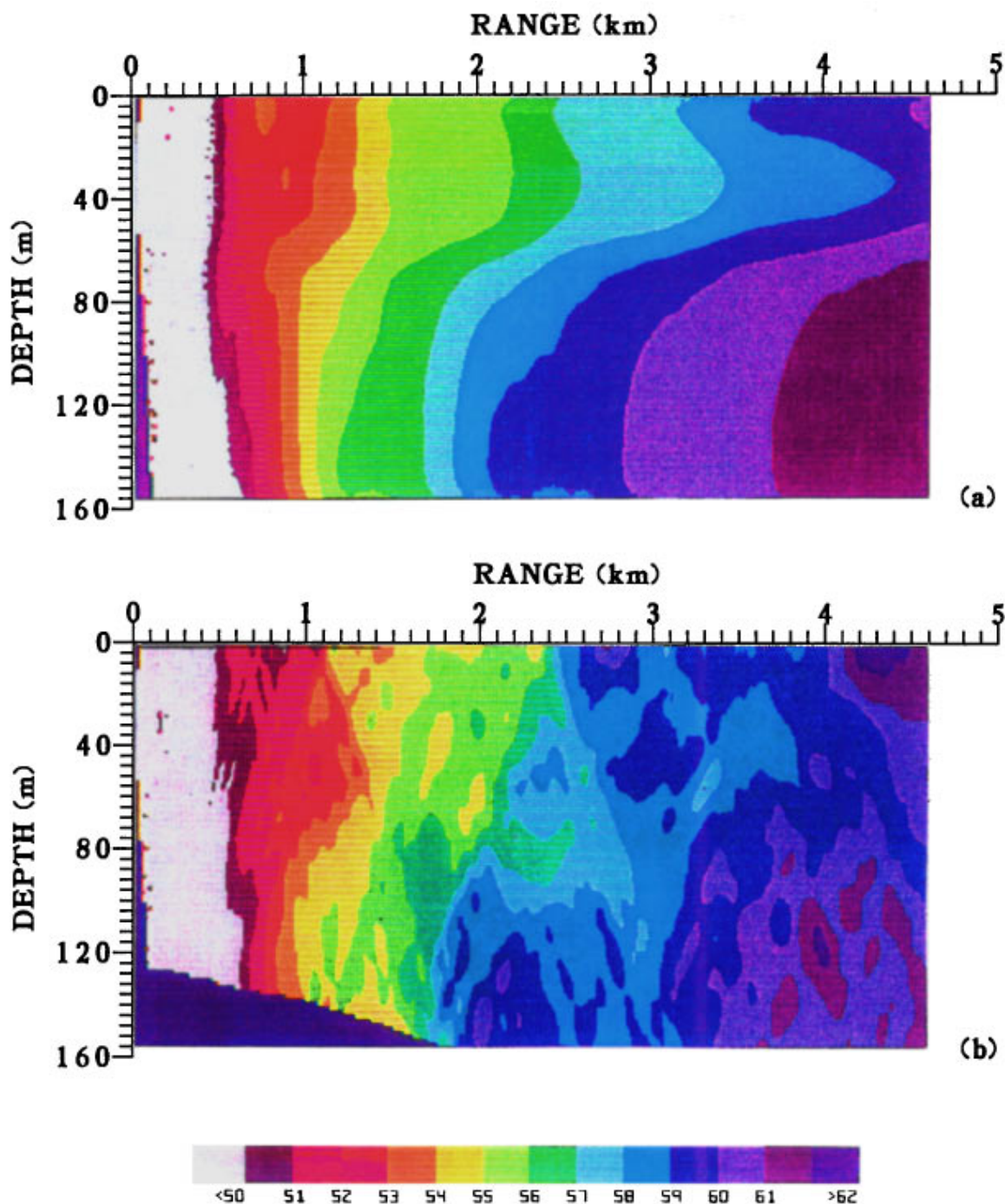


FIG. 16. GRAB propagation loss contours at 1 kHz for a sandy bottom: (a) flat and (b) downslope bathymetry.

III. SUMMARY AND CONCLUSIONS

To summarize, a high-frequency propagation loss model was developed to investigate shallow ocean environments. The model is based on ray tracing, Gaussian ray bundles, and virtual rays. The ray tracing determines ray trajectories, inclination angles, and losses due to volume attenuation and the ocean boundaries along numerous test rays. Gaussian ray bundles replace the classical spreading loss of geometrical acoustics. The area under a ray bundle is chosen to conserve energy, while the algorithm for its standard deviation was derived by fitting results at a smooth caustic. Contributions

from the tails of bundles that extend into the ocean boundaries are recovered by unfolding test rays into virtual rays at the appropriate boundary.

Ray bundles that undergo the same number of surface and bottom reflections are combined into acoustic eigenrays. An eigenray amplitude is simply the power sum of its ray bundles. Weighted sums yield the remaining parameters. The power addition propagation loss at a field point is the power addition of all eigenrays to the point and equals the power addition of the contributing ray bundles. However, the coherent addition propagation loss is the coherent addition of all

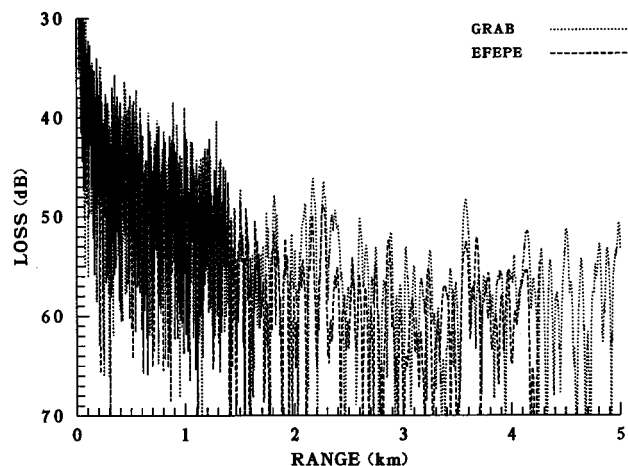


FIG. 17. GRAB and EFEPE propagation loss predictions at 1 kHz for a rock to sand downslope bathymetry.

eigenrays and generally does not equal the coherent addition of the ray bundles.

Although rigorous justification is not currently available, the Gaussian ray bundle method appears to be valid over a larger band of frequencies than originally intended. Its applicability is being established by comparison with various Navy "standards" and at-sea measurements. Results for the classic convergence zone and shallow-water test cases are encouraging.

Future plans include resolving some of the more questionable aspects of the model. In addition to the lack of mathematical rigor, phase errors occur at turning points and caustics. As with many ray-tracing models, the selection of

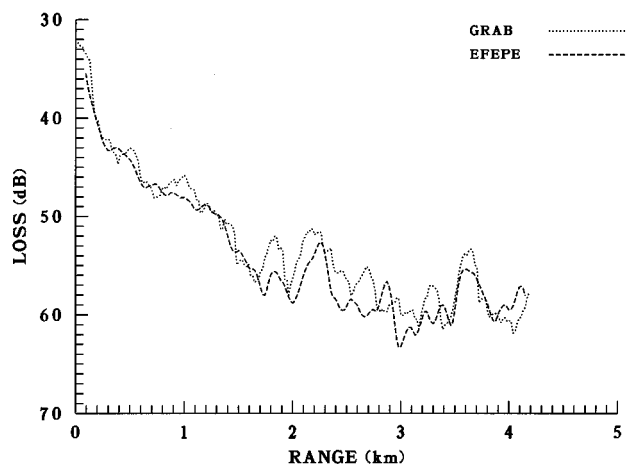


FIG. 18. GRAB and EFEPE range-averaged propagation loss predictions at 1 kHz for a rock to sand downslope bathymetry.

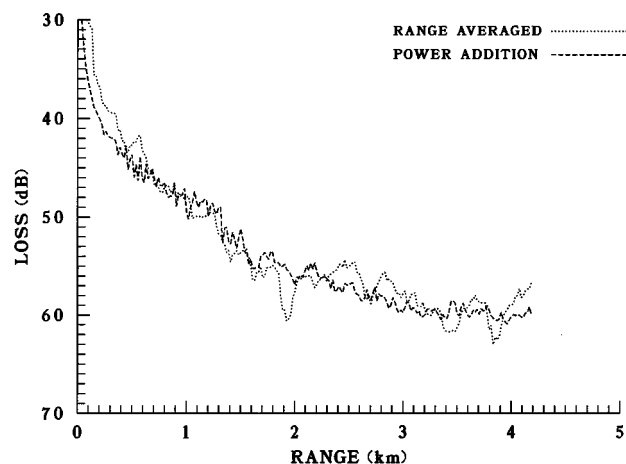


FIG. 19. GRAB power-addition and range-averaged propagation loss predictions at 21 kHz for a rock to sand downslope bathymetry.

test rays is left to the user. Too few may jeopardize fidelity; too many may be costly. Current experience calls for vertical angle increments of 0.1 to 0.01° . Away from caustics, real eigenrays are not sensitive to the lower bound of the ray bundle standard deviation. Since imaginary eigenrays are formed by the tails of Gaussian bundles, and these tails depend on the standard deviation, one should expect shadow zone propagation to be very sensitive to the lower bound. It is not known why the expression for the lower bound is so robust.

ACKNOWLEDGMENTS

This work was sponsored by Dr. J. Simmen, Office of Naval Research, and by F. E. Aidala, Naval Undersea Warfare Center.

- ¹V. Červený and J. E. P. Soares, "Fresnel volume ray tracing," *Geophysics* **57**(7), 902–915 (1992).
- ²M. B. Porter and H. P. Bucker, "Gaussian beam tracing for computing ocean acoustic fields," *J. Acoust. Soc. Am.* **82**(4), 1349–1359 (1987).
- ³M. G. Brown, "A Maslov-Chapman wavefield representation for wide-angle one-way propagation," *Geophys. J. Int.* **116**, 513–526 (1994).
- ⁴H. Davis, H. Fleming, W. A. Hardy, R. Miningham, and S. Rosenbaum, "The Hudson Laboratories ray tracing program," Hudson Laboratories Technical Report No. 150 (1968).
- ⁵L. A. Gainey and E. S. Holmes, "Software Product Specification of the Parabolic Equation V3.4," Scientific Applications International Corp., OAMI-SPS-22 (1992).
- ⁶M. D. Collins, "A split-step Pade solution for the parabolic equation method," *J. Acoust. Soc. Am.* **93**, 1736–1742 (1993).
- ⁷M. A. Pedersen and D. F. Gordon, "Normal-mode and ray theory applied to underwater acoustic conditions of extreme downward refraction," *J. Acoust. Soc. Am.* **51**(1), 323–368 (part 2) (1972).
- ⁸E. Miller, G. Hebenstreit, and R. Keenan, "Sound speed interpolation mechanisms for range-dependent models," Scientific Applications International Corp., 94-1093 (1994).